# Expanding Pore Size of Al-BDC Metal−Organic Frameworks as a Way to Achieve High Adsorption Selectivity for CO_2/CH_4 Separation

Tianjun Sun,* Xinyu Ren, Jiangliang Hu, and Shudong Wang*

Dalian National Laboratory for Clean Energy, State Key Laboratory of Catalysis, Dalian Institute of Chemical Physics, Chinese Academy of Sciences, Dalian 116023, P. R. China

Ⓢ Supporting Information

ABSTRACT: The mesostructured Al-BDC metal−organic frameworks (MOFs) with an average pore size of 2.58 nm were prepared via a simplified washing and drying process and applied to the separation of CO_2/CH_4 mixtures. The adsorption equilibrium and thermodynamics of CH_4 and CO_2 were studied in the dynamic processes by the volumetric−chromatographic and inverse gas chromatographic (IGC) methods. The experiments represent that the Al-BDC MOF with large pore size has a much higher CO_2/CH_4 selectivity of ca. 24 at 303 K in the pressure range 0−1.0 MPa and therefore appears to be a good candidate for the separation of CH_4 from CO_2. The initial heats of adsorption of CH_4 and CO_2 on the mesostructured Al-BDC MOFs were determined to be 11.5 and 25.2 kJ mol^{-1} by the IGC method, respectively, which are significantly reduced by ca. 25% compared with that on the microporous Al-BDC MOFs. The results indicate that the expanded pore size not only greatly increases the selectivity of CO_2 adsorption over CH_4 but also reduces the adsorption heat, revealing that it should be the desired method to obtain a satisfactory absorbent for CO_2/CH_4 separation.
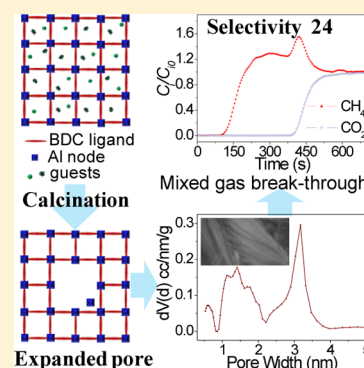
■ INTRODUCTION

Natural gas (NG) is one of the cleanest carbon fuels due to its low CO_2 and particle emissions after combustion and has become one of the fastest growing primary energy sources in the world. The huge demand for natural gas has led to a re-evaluation of the development potential of unconventional, stranded, and contaminated gas reserves, which contain much more than 2% CO_2 (with peaks up to 70 vol %).[1,2] The removal of CO_2 from these NG reserves is critical for natural gas transportation and usage because it significantly reduces the energy content of natural gas and also induces pipeline corrosion.[3]

The amine-based absorption/stripping process has been used for the separation of CO_2 from natural gas for a long time,[4] but the solvents used, such as aqueous alkanolamines, usually require high energy and often lead to environmental issues due to solvent loss and degradation.[5−7] Adsorption-based separation methods, such as pressure swing adsorption (PSA), temperature swing adsorption, and membrane processes, are commonly accepted to be the most efficient and affordable, but adsorbent regeneration is still difficult and energy costly, leading to low productivity and great expense.[1,3,4] Nonetheless, PSA has the advantages of easy control and low energy demand and is considered as one of the better choices for CO_2/CH_4 separation in the future.[8] The vital step in designing PSA processes for the separation of CO_2/CH_4 mixtures is the development of adsorbents with a high CO_2 capacity, good CO_2/CH_4 selectivity, excellent regeneration properties, and high thermal stabilities.

Zeolites,[9−13] activated carbons,[14−18] silicas,[19,20] and new classes of porous materials[21−31] have been investigated for their CO_2 adsorption behaviors. Thereinto, activated carbon and silicas have been widely studied as adsorbents owing to their stability, low polarity, and low energy intensive regeneration operations, and the main drawback is the low selectivity for CO_2/CH_4 separation.[14−18] On the other hand, zeolites are mostly adequate for separating CO_2 from CH_4 due to the preferential adsorption of CO_2 over CH_4 in the polar cavities and channels of relatively aluminum-rich zeolites.[9−13] However, the high affinity of zeolites for CO_2 hinders its desorption, which leads to low productivity and high regeneration energy cost.[13] Clearly, to better satisfy the needs of the CO_2/CH_4 separation, the separation performance of conventional adsorbents, such as zeolite, activated carbons, and silica gels, should be strengthened. Recently, metal−organic frameworks (MOFs) have been emerging as promising materials in applications of adsorption separation, owing to their flexibility to design through control of the architecture and chemical functionality of the pores. Up to date, many different MOFs have been explored to examine their performance on the separation of CO_2/CH_4 gas mixtures, both experimentally and theoretically, such as Zn(bdc)dabco,[21] CPO-27-M(Co, Ni, Zn),[22] Cu-BTC,[23] MIL-53 and MIL-47,[24,28,29] MIL-101-(Al),[25,30] Uio-66,[26] ZIF,[27] Mg-MOF-74,[2] and mixed-ligand MOFs.[31] All of these studies have demonstrated that these

MOFs exhibit high selectivities for CO_2 separation from CO_2/CH_4 mixtures, and the selectivities for CO_2 on some MOFs are more than 10, revealing that MOFs could act as the alternatives of conventional adsorbents for CO_2/CH_4 separation. However, only a few of these MOFs can be synthesized in large scale from low-cost raw materials under available conditions, which is of paramount importance for MOFs becoming a realistic adsorbent for CO_2/CH_4 separation.[26,29] Furthermore, most of the MOFs with higher stability have not exhibited higher selectivity of CO_2 over CH_4 than conventional adsorbents such as zeolites and activated carbons.[11,29]

Very recently, immobilization of functional sites to induce their stronger interactions with carbon dioxide, or control/tune the pore size/curvature to maximize the size-exclusive effects, has been used to improve the CO_2/CH_4 separation selectivities of the above-mentioned adsorbents. For example, amines, the OH group, and Li^+ have been grafted onto surfaces of porous materials to enhance adsorption of the CO_2 molecule on conventional adsorbents and MOFs.[16,19,32−36] In addition, a novel "molecular sieving" effect, which is based on a difference in ability of a guest molecule to induce temporary and reversible cation deviation from the center of pore apertures, has been uncovered on Cs^+-containing chabazite zeolites.[37] Obviously, these modified adsorbents have much higher affinity to CO_2, and some of them exhibit record high selectivity for separation of CO_2/CH_4 mixtures.[32,37] Unfortunately, specific interactions of adsorbed CO_2 molecules with the surfaces increase the selectivity of CO_2 adsorption over CH_4 while reducing the regenerability of adsorbents; that is, the regeneration property of adsorbents must be considered while enhancing CO_2/CH_4 selectivity by the method of modification.

On the basis of the above analysis, the desired adsorbent for CO_2/CH_4 separation should have a high CO_2 capacity, high selectivity, and the fitting affinity to CO_2. Although a lot of MOFs have been employed to study the CO_2 selectivity over CH_4, it is still far from satisfactory for natural gas upgrading owing to many reports limited to single-component measurements or simulations. In the present work, we report the enhanced adsorption behavior of CO_2 over CH_4 on Al-BDC MOFs by the increased pore sizes. First, Al-BDC MOFs were prepared via a simple method fit for industrial use, and the pore size of Al-BDC MOFs was enlarged by a simplified washing and drying process. Subsequently, the adsorption equilibrium and thermodynamics of CH_4 and CO_2 were studied in the dynamic process by the volumetric−chromatographic and inverse gas chromatographic (IGC) methods.

■ EXPERIMENTAL SECTION

Materials. The Al-BDC MOF material studied in this work was synthesized according to the previously reported modus operandi.[28,38] In a typical synthesis, 40 g of $Al(NO_3)_3$·$9H_2O$ and 52 g of 1,4-benzenedicarboxylate (H_2BDC) were dissolved in a 600 mL of DMF. The resulting stock solution was decanted into ten 120 mL Teflon-lined stainless steel autoclaves, which were capped tightly and heated to 160 °C in an oven. After the reaction under the autogenous pressure for 12 h, the products were allowed to cool to room temperature. The white precipitate was isolated from the mother liquor by filtration and washed thoroughly with 200 mL of DMF and then immersed in 200 mL of fresh methanol to exchange the DMF over 12 h and then washed with 200 mL of methanol. The as-produced samples were then evacuated to

dryness at 100 °C for 4 h and designated as $AlBDC_{Syn}$. The sample $AlBDC_{Syn}$ was divided into two parts. One part continued to remove the guest molecules incorporated in the crystals under a dynamic vacuum at 180 °C for 12 h, yielding yellowish powders and designated as $AlBDC_{Evac}$. The other part of $AlBDC_{Syn}$ and $AlBDC_{Evac}$ samples was finally heated to 350 °C at a rate of 1 °C/min and treated for 45 h in a muffle furnace, defined as $AlBDC_{Meso}$ and $AlBDC_{Micro}$, respectively.

Al-BDC MOF pellets were prepared from the as-produced powders through a binder-free forming process, which was conducted by a tablet press applying a mechanical pressure of 60−70 atm. The obtained pellets were crushed and sieved to the particles with the average size of 80 μm that were then used as adsorbents.

Materials and Adsorbent Characterization. The X-ray powder diffraction (XRD) measurements were conducted for 2θ values from 5° to 65° on a Rigaku RINTD/MAX-2500PC diffractometer (Cu Kα, 40 kV, 100 mA) with a step size of 0.02°.

The Fourier transform infrared (FT-IR) spectroscopy was performed on a Nicolet 6800 equipment with an MCT-A detector cooled by liquid nitrogen. IR spectra were collected by recording 32 scans at a resolution of 6 cm^{-1} in the region of 4000−650 cm^{-1} with samples in potassium bromide pellets.

Surface area and pore characteristics of the Al-BDC MOFs were confirmed by the N_2 physisorption measurements at 77 K on a volumetric sorption analyzer Autosorb-iQ2 from Quantachrome Instruments U.S. equipped with a high-resolution pressure sensor. The experimental apparent specific surface area, the total pore volume, and pore size distributions (PSDs) were calculated from these adsorption isotherms. Prior to analysis, the Al-BDC sample was outgassed at 180 °C under dynamic vacuum for 12 h.

The thermal stability of the Al-BDC MOFs was studied by thermogravimetric analysis (TGA) coupled with differential scanning calorimetry (DSC), which was carried out in air (20 mL min^{-1}, 30−800 °C, 10 °C min^{-1}) using a NETZSCH STA 449 F3 analyzer. In the TGA run, a Pfeiffer vacuum OmniStar mass spectrometer was used to investigate the chemical nature of the species leaving the sample.

^{13}C solid-state NMR measurements were performed on a Varian Infinityplus-400 spectrometer equipped with a 5 mm magic angle spinning (MAS) probe at a resonance frequency of 100.5 MHz with a spinning rate of 8 kHz. ^1H−^{13}C CP/MAS NMR spectra were performed with a contact time of 2 ms, a recycle delay of 2 s, and 2100 scans. SEM images of the Al-BDC MOFs were obtained on an FEI Quanta 200F microscope operated at 60 Pa and 30 kV. The sample was fixed on a copper holder with conductive adhesives. In addition, the density of Al-BDC MOF pellets was measured by the conventional mercury intrusion method.

Binary Gas Breakthrough Curve Measurements. CH_4/CO_2 breakthrough curves were obtained on a homemade gas-flow apparatus (Figure S1, Supporting Information), allowing one to perform measurements from atmospheric pressure up to 1.0 MPa. Flow rates of He (prepurified, 99.99%), CH_4 (99.5%), and CO_2 (bone dry 99.8%) were controlled using Brooks 5850e mass flow controllers. For CH_4/CO_2 breakthrough experiments, 3.5 mL of the Al-BDC MOF sample was loaded into a stainless steel column and then installed onto the gas-flow apparatus under flowing He. Before each breakthrough experiment, the sample in the column was activated and outgassed in a heating mantle at 473 K for 2 h under a helium

flow. The CH_4/CO_2 breakthrough experiments were conducted at 303 K with constant gas mixture composition, and the effluent was analyzed using an Ameitek Dycor mass spectrometer. The signal strength of the mass spectrometer has a good linear relationship with the molar concentration of gas in the range 0−15%. For all experiments, a certain amount of He, that is 40 times the quantity of feed gas, was introduced to control the molar concentration of gas into the mass spectrometer. The sample column was first purged with He after finishing the adsorption step in every measurement. The pressure drop over the column was always less than 0.005 MPa. The selectivity is calculated as

$$a_{i,j} = \frac{C_i/y_i}{C_j/y_j} = \frac{C_i/C_j}{y_i/y_j} \tag{1}$$

where $\alpha_{i,j}$ is the adsorption selectivity; C_i is the adsorbed amount of compound i; and y_i is the mole fraction of compound i in the gas phase.

For validation of the setup, additional adsorption measurements with CH_4/CO_2 binary mixtures at 303 K under different pressure on micropore-activated carbon, ZIF-8, and Cu-BTC MOFs were carried out. Very good agreement between literature data and the results of this study was obtained.

Inverse Gas Chromatography Experiments. Adsorption equilibrium and thermodynamics of CO_2 and CH_4 on Al-BDC MOFs were studied by an inverse gas chromatographic (IGC) method, which was carried out on an Agilent 4890 gas chromatograph with a thermal conductivity detector (Figure S2, Supporting Information). The adsorbent was placed into a 40 cm length of the 304 stainless steel column, with passivated inner walls and an inside diameter of 3 mm (o.d. = 4 mm). To obtain homogeneous packing, the adsorbent (80/100 mesh) was introduced in small quantities, accompanied by mechanical vibration, and the two ends of the column were then plugged with silica wool.

Prior to experiment, the column was stabilized on the GC system at 200 °C for 4 h under an argon flow rate of 20 mL/min. Measurements were carried out in the temperature range of 30−70 °C. Argon was used as carrier gas, and flow rates were measured using a calibrated soap bubble flowmeter. To meet the requirements of adsorption at infinite dilution, the symmetry of the peaks and reproducible retention times, amounts of injected samples were controlled accurately by a calibrated loop of 0.23 mL. For each measurement, at least three repeated injections were taken, obtaining reproducible results. The injected probe molecule was interacted with adsorbent during the transport by carrier gas through the column, and then a chromatographic peak was detected with the specific retaining value and peak form. From the evaluated retention time (t_R, min) and flow rate (F, mL/min) of the carrier gas, the retention volume (V_R, mL) was calculated.

■ RESULTS AND DISCUSSION

Characterization of the Al-BDC MOFs. The N_2 adsorption isotherms of the Al-BDC MOF samples at 77 K are shown in Figure 1. The BET surface area of the AlBDC$_{Syn}$ and AlBDC$_{Evac}$ MOFs is ca. 1100 m^2 g^{-1}, and the micropore volume is ca. 0.35 cm^3 g^{-1}. After being calcined at 350 °C, the BET surface area and micropore volume of the AlBDC$_{Micro}$ sample increase to ca. 1400 m^2 g^{-1} and 0.497 cm^3 g^{-1}, respectively. However, the BET surface area and micro-/mesopore volume of the AlBDC$_{Meso}$ sample were ca. 700 m^2
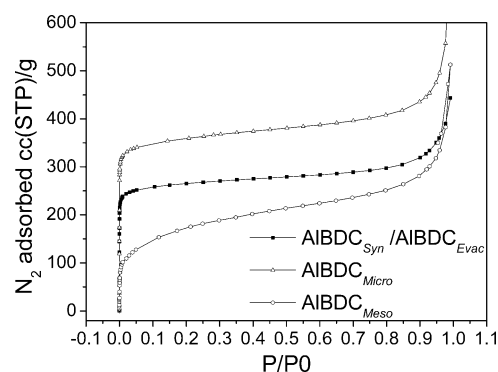

Figure 1. Nitrogen-sorption isotherms for the Al-BDC MOFs at 77 K up to 1 bar.

g^{-1} and 0.396 cm^3 g^{-1}, respectively. Obviously, the pore volumes of Al-BDC samples can be increased by the drying and calcination, and their surface areas depend on the specific washing and drying conditions. The pore size distributions of the AlBDC$_{Micro}$ and AlBDC$_{Meso}$ samples are depicted in Figure 2, which is based on the NLDFT model for cylinder pore geometry. This analysis shows that the average pore size of AlBDC$_{Micro}$ samples is ca. 0.86 nm (shown in Figure 2a), which is close to the reported MIL53(Al).[28] Figure 2b shows that the pore size distribution of the AlBDC$_{Meso}$ samples is ca. 2.58 nm, which is 3 times more than that of AlBDC$_{Micro}$ samples.

The IR spectra of the Al-BDC MOFs are shown in Figure 3 and Figure S3 (Supporting Information), displaying the similar profiles of all IR spectra. As can be seen, the as-synthesized and extracted Al-BDC MOFs present similar profiles, implying a similar surface functionality. The peaks in the usual region of 1400−1700 cm^{-1} are associated with vibrational bands of the carboxylic function.[28] In curve A, the IR band near 1670 cm^{-1} can be assigned as the C=O stretching mode of the free H_2BDC molecules trapped in the pores of the AlBDC$_{Syn}$ MOF, while the absorption bands located at around 1070−1200 cm^{-1} can be attributed to the N−CH$_3$ bending mode of the DMF encapsulated in the AlBDC$_{Syn}$ MOF. It should be noted that it is really difficult to detect methanol in the IR spectrum because of the serious interferences from other functional groups in the AlBDC$_{Syn}$ MOF. In curves B−F, the characteristic peaks of the free H_2BDC and DMF molecules are not found, which reveals that the free H_2BDC and DMF molecules have been removed in the AlBDC$_{Evac}$, AlBDC$_{Meso}$, and AlBDC$_{Micro}$ samples. Moreover, the absorption bands, located at around 1110 and 1300 cm^{-1} in curves B−F, can be attributed to the vibrational bands of C−C(=O) and C(=O)-O, and the intense −COO$^-$ in-plane bending mode can be observed around 755 cm^{-1}. The aromatic C−H stretching vibrations shift to the region around 2850−3000 cm^{-1} owing to the formation of the oxo-bridged Al-BDC carboxylate, while the aromatic C−H out-of-plane bending vibrations appear at 835 and 880 cm^{-1}. In addition, a broad vibrational band at the region of 3100−3725 cm^{-1} corresponds to the bending and stretching modes of the intercrystalline water and physisorbed water. Comparing these curves in Figure 3, it can be found that the characteristic peaks of water in the AlBDC$_{Syn}$ and AlBDC$_{Meso}$ samples disappear after vacuum or high-temperature degassing (see curves B and D in Figure 3). However, curve F in Figure 3 shows that the band at the region of 3100−3725 cm^{-1} of the degassed AlBDC$_{Micro}$ samples is still strong, revealing that the interaction of water and AlBDC$_{Micro}$ MOFs is enhanced greatly.
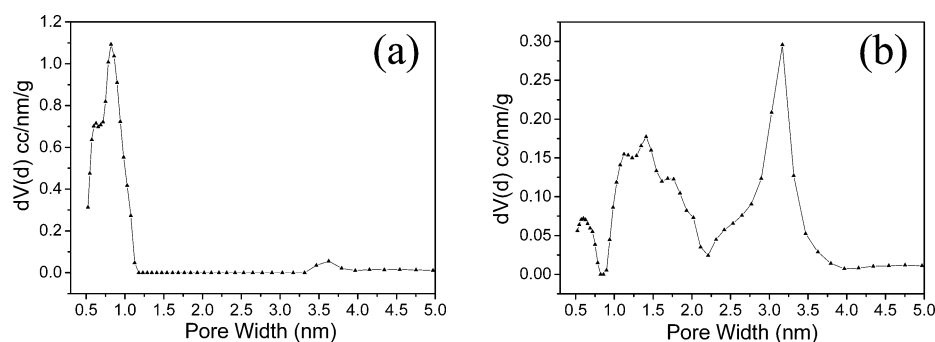
Figure 2. Pore-size distributions of the AlBDC$_{Micro}$ and AlBDC$_{Meso}$ MOFs calculated by the NLDFT.
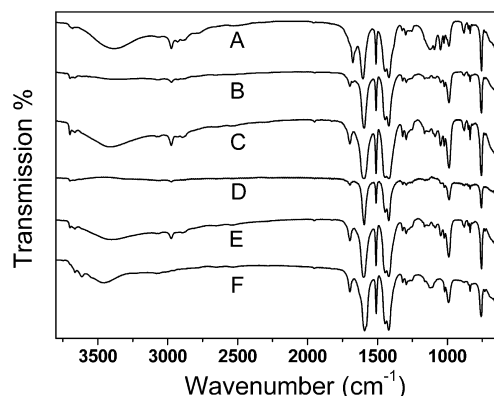

Figure 3. FT-IR spectra of the Al-BDC MOFs: (A) AlBDC$_{Syn}$; (B) AlBDC$_{Evac}$; (C) AlBDC$_{Meso}$; (D) activated AlBDC$_{Meso}$ at 200 °C; (E) AlBDC$_{Micro}$; (F) activated AlBDC$_{Micro}$ at 200 °C.

^{13}C NMR spectroscopy is an effective way to detect the missing guest molecules by IR spectra, and the ^{1}H−^{13}C CP/MAS NMR spectra of the Al-BDC MOFs are displayed in Figure 4. The signals at ca. 128 and 137 ppm are attributable to the CH units and the quaternary carbons of the aromatic carbons, and the signals in the region 169−177 ppm can be assigned to the carbons of the carboxylic functions in both the protonated (the carboxylate groups with occluded BDC ligands, δ = 171−172 ppm) and deprotonated forms (the carboxylate groups, δ = 174−175 ppm).[39,40] The three signals

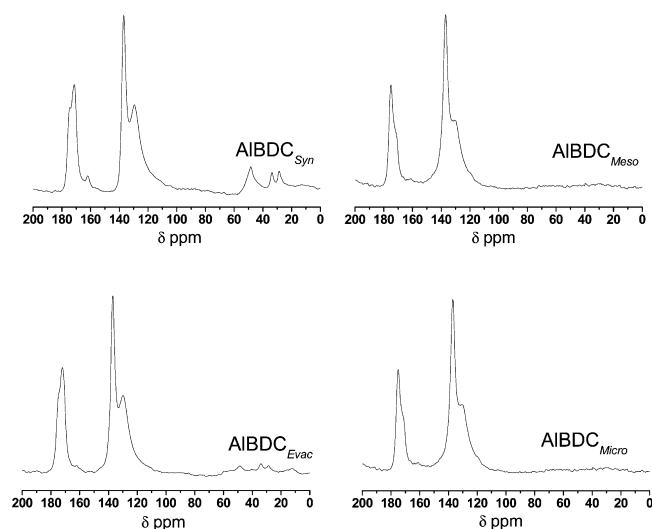**Figure 4.** ^{1}H−^{13}C CP/MAS NMR spectra of the Al-BDC MOFs.

at 28.5, 34.5, and 162 ppm can be assigned to carbons of the two −CH$_3$ and −COH groups of DMF, and the peak at 49 ppm is the characteristic peak of CH$_3$OH. Clearly, the AlBDC$_{Syn}$ sample contains many free CH$_3$OH, DMF molecules and the occluded BDC ligands, except a little free H$_2$BDC. Moreover, the amounts of DMF and methanol in the AlBDC$_{Evac}$ sample decrease greatly after degassing at 180 °C, and these free guest molecules are not found in the AlBDC$_{Micro}$ and AlBDC$_{Meso}$ MOFs. It is interesting to note that the resonance of the carboxylate groups with occluded BDC ligands in the AlBDC$_{Syn}$ sample shifts from 171.3 to 172.2 ppm after degassing at 180 °C, and the resonance of the carboxylate groups is dominant after calcination in air at 350 °C, as shown in Figure S4 (Supporting Information). These results suggest that some occluded BDC ligands should be eliminated or recrystallized to the other form in the frameworks after the post-treatment process.

The X-ray powder diffraction patterns of the as-synthesized and extracted samples are shown in Figure 5, indicating these
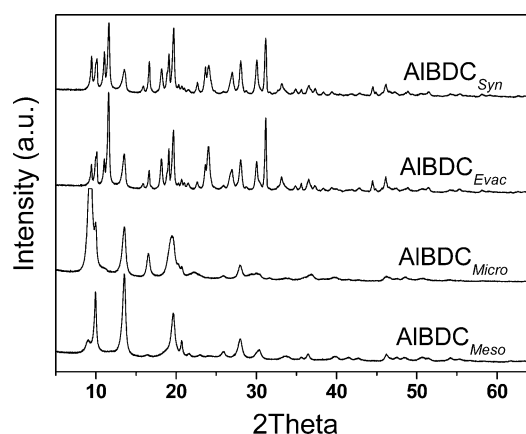

Figure 5. XRD patterns of the Al-BDC MOFs.

materials have well-crystalline structures. Apparently, the diffraction peaks of these materials are not identical with the MIL-53(Al) reported earlier by Ferey et al.,[28] and the obtained peaks of AlBDC$_{Syn}$ and AlBDC$_{Evac}$ are distinctly different from the extracted samples (AlBDC$_{Micro}$ and AlBDC$_{Meso}$ MOFs). Compared with the typical MIL-53(Al), the slight difference of the AlBDC$_{Syn}$ sample could be due to the presence of free H$_2$BDC molecules inside the pores and the metastable phase of BDC and Al^{3+} (occluded BDC ligands), resulting from the different condition of the crystal growth. XRD analysis of the AlBDC$_{Syn}$ sample identifies H$_2$BDC and its metastable phase at ca. 2θ 11.0, 11.5, 18.2, 19.0, 24.1, 27.0, 30.0, and 31.2° (JCPDS

card No. 03-0127 and No. 21-1919).[28,29] In the XRD pattern of AlBDC$_{Evac}$ MOFs, there are obvious changes at 2θ 11.0, 11.5, 24.1, 30.0, and 31.2° with the evacuation of guest moleculars (DMF, methanol, and H$_2$BDC) under vacuum at 180 °C, revealing that the occluded BDC ligands are not stable in the AlBDC$_{Syn}$ sample. Therefore, the diffraction peaks of the occluded BDC ligands disappear after calcination. As can be seen from Figure 5, the characteristic peaks of AlBDC$_{Micro}$ and AlBDC$_{Meso}$ MOFs are similar to the results reported by Müller et al.,[38] but there are significant differences between them at ca. 2θ 9.0–10.2, 16.5, 20.9, and 28.0°. Actually, it can be seen clearly from Figure 5 that there are no changes in the peak positions of the AlBDC$_{Micro}$ and AlBDC$_{Meso}$ crystals, implying that they have the same crystal structure. However, the intensity of the XRD peaks at 9.0–10.2° and 13.5° is different, which should be attributed to the different morphologies and exposed planes of crystals because of the different treatment methods of the samples. It should be noted that the peaks at 2θ 16.4, 20.1, and 28.0° of the AlBDC$_{Micro}$ MOF indicate the existence of the gibbsite in this sample (JCPDS card No. 02-0173), whereas the peaks at 2θ 10.2, 20.9, and 28.0° of the AlBDC$_{Meso}$ MOF imply that the amorphous Al$_2$O$_3$ appears in this sample (JCPDS card No. 31-0026). More specifically, many BDC linkers were eliminated from the framework, and some crystals were transformed into amorphous Al$_2$O$_3$ in the calcination of the AlBDC$_{Syn}$ sample at 350 °C, which could result in the split and expansion of some defined micropores. On the other hand, the evacuation of the guest molecules could induce the crystal transition or recrystallization of the occluded BDC molecules at 180 °C, which enhances the thermostability of the AlBDC$_{Evac}$ crystals.

Table 1. Properties of the AlBDC$_{Micro}$ and AlBDC$_{Meso}$ MOFs

sample	AlBDC$_{Micro}$	AlBDC$_{Meso}$
BET surface area (m^2/g)	1419	689
pore volume (cc/g, $P/P_0 = 0.35$)	0.497	0.396
pore size (nm, NLDFT)	0.86	2.58
particle density (g/cm^3)	0.72	1.13
void fraction of pellet θ	0.523	0.511

The thermal stabilities of the Al-BDC MOF samples were investigated by using thermal analysis (TGA) from 30 to 800 °C, and weight loss profiles are presented in Figure 6. In the analysis, the typical ion species of $m/z = 29, 31$ (CH$_3$OH), $m/z = 42, 73$ (DMF), and $m/z = 50, 74$ (C$_6$H$_4$) were monitored at the outlet of the TG analyzer. As for the AlBDC$_{Syn}$ sample, there are two clear weight loss steps in air. The first weight loss
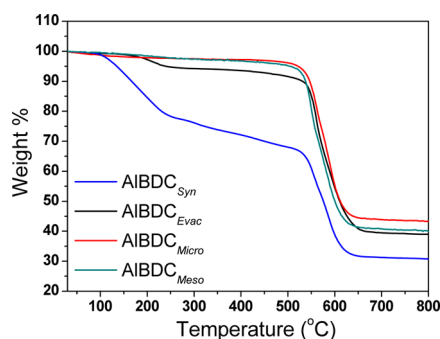

Figure 6. TG curves of the Al-BDC MOFs.

of ca. 33% from 80 °C is observed, and ion species of CH$_3$OH, DMF, and BDC ligands appear in turn with the increase of temperature in the MS profiles, as shown in Figure S5 (Supporting Information). Obviously, the weight loss below 200 °C is due to the release of methanol and a little DMF, whereas the weight loss above 200 °C is because of the DMF and some BDC ligands removal. The second weight loss of ca. 35% starts from 520 °C, and the MS curves show the intense peaks at $m/z = 50.74$ that correspond to the collapse of the framework. That is to say, the Al-BDC framework is thermally stable up to 500 °C, which can completely satisfy the requirements for the application as adsorbents. The degassed AlBDC$_{Evac}$ sample shows weight loss process at a similar temperature (at 100 °C ca. 8%, at 520 °C ca. 48%), indicating that a lot of guest molecules have been degassed at 180 °C under vacuum. The similar weight loss processes are also observed for AlBDC$_{Micro}$ and AlBDC$_{Meso}$ samples; however, the weight loss at 100 °C is less than 5%, and the weight loss at 500 °C is up to 50%. In addition, a very small difference can be observed from the curves of the AlBDC$_{Micro}$ and AlBDC$_{Meso}$ samples at low temperature, where the weight loss of the AlBDC$_{Micro}$ samples is ca. 2.5% and is half that of the AlBDC$_{Meso}$ samples. In the case of the AlBDC$_{Evac}$, AlBDC$_{Micro}$, and AlBDC$_{Meso}$ samples, the MS detector has captured nothing but the ion species of BDC ligands between 500 and 600 °C in the TGA run, as shown in Figure S6 (Supporting Information).

To further explain the formation of the mesopores in Al-BDC MOFs, TG–DSC–MS analyses of the AlBDC$_{Syn}$ and AlBDC$_{Evac}$ samples were conducted. In the DSC curve of the AlBDC$_{Syn}$ MOF, two exothermic processes can be distinguished, as shown in Figure 7. The first exothermic process occurs between 200 and 400 °C, including two weak peaks at 230 and 330 °C, respectively. The second exothermic process appears above 500 °C, corresponding to the strong exothermic combustion reaction of the AlBDC$_{Syn}$ framework. Apparently, the exothermic quantity at low temperature is much less than that at high temperature, implying that it does not take complete combustion to form CO$_2$ and H$_2$O below 400 °C. Combining the TG–MS and TG–DSC results of the AlBDC$_{Syn}$ sample, it can be concluded that the volatization, pyrolysis, and combustion of the free guest molecules and some occluded BDC ligands should take place simutaneously below 400 °C under air, which also decreases the heat release to some extant. On the basis of the TG–MS and ^{13}C NMR results, the exothermic peak at 330 °C should be attributed to the decomposition of some occluded BDC ligands, which could result in the expansion of micropores in the AlBDC$_{Syn}$ sample. As a comparison, there is no distinct exothermic peak, and the typical CO$_2$ MS peak ($m/z = 44$) is below 400 °C for the AlBDC$_{Evac}$ sample (shown in Figure 7), revealing that the decomposition of the occluded BDC ligands in calcination of the AlBDC$_{Evac}$ sample is much less than that of the AlBDC$_{Syn}$ sample. In other words, the volatization, pyrolysis, and combustion of the guest molecules and some occluded BDC ligands induce the formation of mesopores during calcination of the AlBDC$_{Syn}$ sample.

Figure 8a and 8b shows the SEM images of the AlBDC$_{Micro}$ and AlBDC$_{Meso}$ samples prepared in this work, respectively. It can be seen that the AlBDC$_{Micro}$ crystals are cone-like particles with an average length of ca. 4 μm and diameter of ca. 2.5 μm. However, the AlBDC$_{Meso}$ crystals are like cleavage from AlBDC$_{Micro}$ crystals, which are much slighter and thinner. As above-mentioned, the different shape and size between
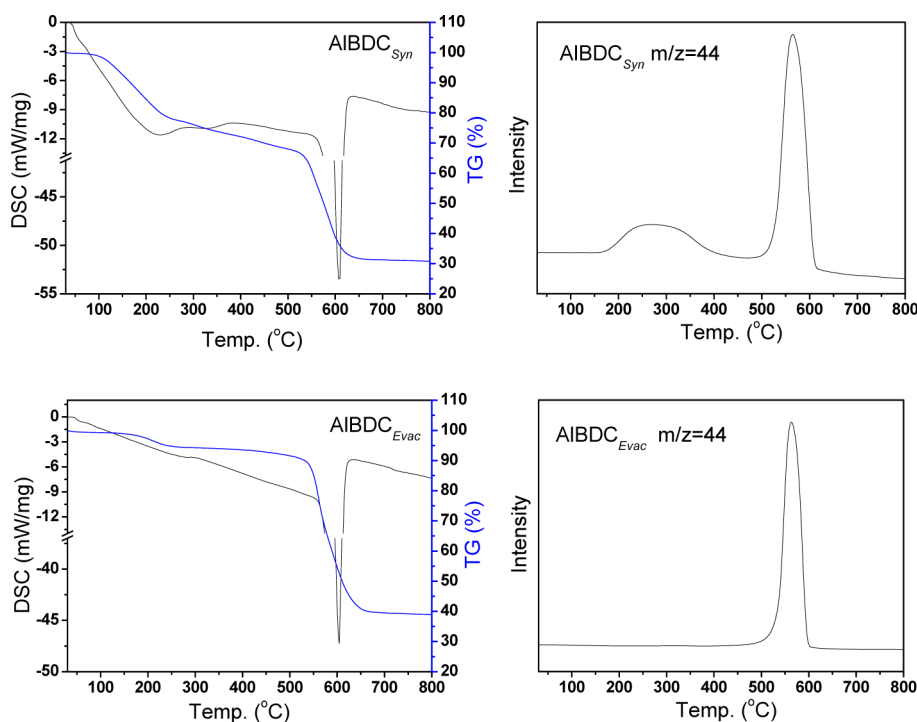
Figure 7. TG−DSC curves and MS profiles of CO_2 ($m/z = 44$) during calcination under air for the $AlBDC_{Syn}$ and $AlBDC_{Evac}$ MOFs.
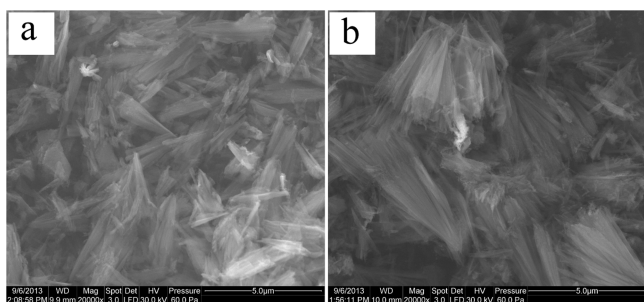

Figure 8. SEM images of the $AlBDC_{Micro}$ (a) and $AlBDC_{Meso}$ (b) MOFs.

$AlBDC_{Meso}$ and $AlBDC_{Micro}$ crystals could result in the variation of relative intensity of diffraction peaks in their XRD patterns. All these findings in N_2 adsorption, IR, NMR, XRD, and TG−DSC−MS experiments allow us to conclude that the formation of a mesoporous structure should be attributed to the decomposition of the occluded BDC ligands in the $AlBDC_{Syn}$ crystals and the corresponding split of the defined micropores. More significantly, the mesostructured $AlBDC_{Meso}$ sample has a relatively lower adsorption potential compared with the $AlBDC_{Micro}$ samples owing to its bigger pore size.

Adsorption Equilibrium and Thermodynamics of CH_4 and CO_2. The isosteric heat of adsorption of gas was calculated to evaluate the separation potential of adsorbents. IGC is a more reliable method to evaluate adsorption heats at zero coverage because it has much higher sensitivity than any other technique over the infinite dilution region where the heat can be very sensitive to small changes in coverage.[41] From IGC experimentation, the net retention volume (V_N) can be calculated from the retention time using the flow rate of the carrier gas and compressibility correction factor,[41] and the specific retention volume, V_S, is obtained from the expression $V_S = V_N/Sm$, where S is the specific surface area and m the mass

of adsorbent. The procedures used for the calculation of adsorption enthalpies from IGC experiments have been described in detail in the previous works.[42] The enthalpy of adsorption, ΔH_{ads}, can be derived from the temperature dependence of the specific retention volume at the infinite dilution region, from the following expression

$$\ln V_S = -\frac{\Delta H_{ads}}{RT_c} + \text{Constant} \qquad (2)$$

where V_S is the specific retention volume; T_c is the column temperature; and R is the gas constant. A plot of $\ln V_S$ versus $1/RT_c$ yields ΔH_{ads} as the slope. Because the specific retention volume is in direct proportion to the relative retention time ($t_R - t_m$) of the adsorbate, the plot of $-R \ln(t_R - t_m)$ versus $1/T_c$ must yield ΔH_{ads} as the slope.

Figure 9 shows the plots of $-R \ln(t_R - t_m) = f(1/T_c)$, in which the relative retention times ($t_R - t_m$) of CH_4 and CO_2 were measured over a small temperature range (from 30 to 65 °C) on the $AlBDC_{Micro}$ and $AlBDC_{Meso}$ samples. The

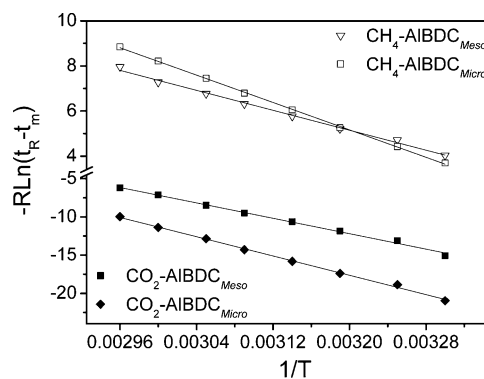**Figure 9.** Linear relationship of $-R \ln(t_R - t_m)$ vs $1/T$ for CH_4 and CO_2 on the $AlBDC_{Micro}$ and $AlBDC_{Meso}$ MOFs.

correlation coefficients of these plots are better than 0.99 in the whole temperature range, especially in the case that CH_4 adsorption is up to 0.999. The deviation at low temperature for CO_2 adsorption on $AlBDC_{Micro}$ samples, however, is due to the enhancement of its adsorption in micropores at lower temperatures. According to eq 2, ΔH_{ads} values of CH_4 and CO_2 adsorption on the $AlBDC_{Micro}$ and $AlBDC_{Meso}$ MOFs were calculated, respectively, as shown in Table 2. It is observed that

Table 2. Adsorption Heats of CH_4 and CO_2 on the $AlBDC_{Micro}$ and $AlBDC_{Meso}$ MOFs

adsorbent	sorbate	
	CH_4	CO_2
$AlBDC_{Micro}$	−15.286	−32.226
$AlBDC_{Meso}$	−11.103	−25.265

the adsorption enthalpies (ΔH_{ads}) of CH_4 and CO_2 on the Al-BDC MOFs are greater than their enthalpy of condensation. The differences between the enthalpies of adsorption and condensation range from 2.9 to 16.8 kJ mol^{-1}, which correspond to the weak energy bonds such as dipole−dipole interactions.

In Table 2, the ΔH_{ads} of CH_4 on the $AlBDC_{micro}$ MOFs is −15.286 kJ mol^{-1}, which is consistent with the reported value in the literature,[28,45] revealing the IGC method is suitable to estimate the adsorption enthalpies. From Table 2, it can be seen that CO_2 exhibits more negative ΔH_{ads} than the corresponding values for CH_4 on the Al-BDC MOFs. The more negative ΔH_{ads} of CO_2 demonstrates its greater interaction with adsorbents owing to the higher molecular polarity of CO_2. In addition, the ΔH_{ads} of CO_2 on the $AlBDC_{Meso}$ samples is ca. 25.26 kJ mol^{-1} and is less than 25% of that on the $AlBDC_{Micro}$ samples. It should be noted that the adsorption enthalpy of CO_2 on the $AlBDC_{Meso}$ MOFs is similar to the microporous active carbon (BPL 25 kJ mol^{-1}),[14] which should be attributed to its large pore size.

Compared with the conventional gravimetric or volumetric methods, the inverse gas chromatograph has been considered as a faster and easier way to study the equilibrium of sorption in biporous adsorbents because a pulse experiment represents (quasi-)equilibrium values at the lower flow rate.[41,43,44] Useful mathematical models for the first absolute moments (the relative retention times ($t_R - t_m$) of the adsorbate) of the chromatographic peaks for the biporous structured adsorbents, which are developed elsewhere,[43,44] are described as

$$t_R - t_m = \frac{L}{v}\left\{1 + \left(\frac{1-\varepsilon}{\varepsilon}\right)K_p\right\} \tag{3}$$

where $K_c = (K_p - \theta)/(1 - \theta)$; v is the interstitial gas velocity; L and ε are the length and the void fraction of the bed; θ is the void fraction of the pellet; and K_c and K_p are the sorption equilibrium constant based on sorbate concentration in a crystal and a pellet of adsorbents, respectively. Obviously, the equilibrium constant can be calculated directly from the first moment of the obtained chromatographic peak.

In the whole experiment, gas velocities were sufficiently low that the pressure drop through the column was very small. According to eq 3, a plot of the first moment vs $1/v$ should be a straight line, and the plots of the first moment obtained from the chromatographic curves are given in Figure 10 for CH_4 and CO_2 adsorption on the $AlBDC_{Micro}$ and $AlBDC_{Meso}$ MOFs. The
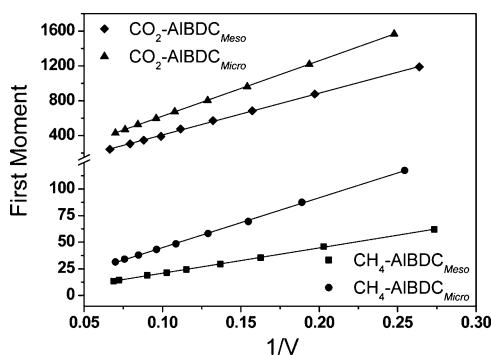

Figure 10. Linear relationship first moment vs $1/v$ of CH_4 and CO_2 on the $AlBDC_{Micro}$ and $AlBDC_{Meso}$ MOFs at 303 K.

correlation coefficients of these plots are better than 0.99, which completely fulfills the linearity requirement. The sorption equilibrium constants of CH_4 and CO_2 calculated from the chromatographic response, according to eq 3, are shown in Table 3. First, the equilibrium constant of methane

Table 3. Chromatographic Adsorption Constants of CH_4 and CO_2 on $AlBDC_{Micro}$ and $AlBDC_{Meso}$ MOFs Calculated from the First Moment

adsorbent	sorbate	K_p	K_c	selectivity
$AlBDC_{Micro}$	CH_4	7.27	14.14	15.9
	CO_2	107.71	224.71	
$AlBDC_{Meso}$	CH_4	4.03	7.20	27.3
	CO_2	96.92	197.15	

on $AlBDC_{Micro}$ samples agrees well with the previously reported gravimetric value,[23,45] thus confirming the validity of the experiment. Second, the sorption equilibrium constant of CH_4 on the $AlBDC_{Meso}$ samples is much lower than that on the $AlBDC_{Micro}$ samples, which should be attributable to its large pore size with low potential field. The sorption equilibrium constants of CO_2 on the adsorbent with different pore sizes, however, are similar, which should be due to the high polarity of CO_2. In addition, the adsorption selectivity in the equilibrium state can be estimated from the ratio of the equilibrium constants.[44] As shown in Table 3, the selectivities of CO_2/CH_4 on the $AlBDC_{Micro}$ and $AlBDC_{Meso}$ MOFs can be calculated as 15.9 and 27.3, respectively.

Binary Mixture Adsorption. Adsorption breakthrough experiments were carried out at 303 K to evaluate the separation performance of the prepared adsorbents in the real CO_2/CH_4 mixtures and to confirm the effect of mesopores for CO_2/CH_4 mixture separation. CO_2−CH_4 mixtures (50−50) were tested at six pressures (0.1, 0.2, 0.4, 0.6, 0.8, and 1.0 MPa) on the $AlBDC_{Micro}$ and $AlBDC_{Meso}$ MOFs, and the adsorption selectivities were calculated according to eq 1. The selectivities of CO_2/CH_4 on the $AlBDC_{Micro}$ and $AlBDC_{Meso}$ MOFs are ca. 12 and 24, respectively, as shown in Table 4. The CO_2/CH_4

Table 4. Adsorptive Separation Performance of CO_2/CH_4 on the $AlBDC_{Micro}$ and $AlBDC_{Meso}$ MOFs at 303 K

adsorbent	pressure (MPa)					
	0.1	0.2	0.4	0.6	0.8	1.0
$AlBDC_{Micro}$	10.5	11.4	11.2	11.7	11.1	10.3
$AlBDC_{Meso}$	25.2	23.8	22.7	24.3	26.3	22.5

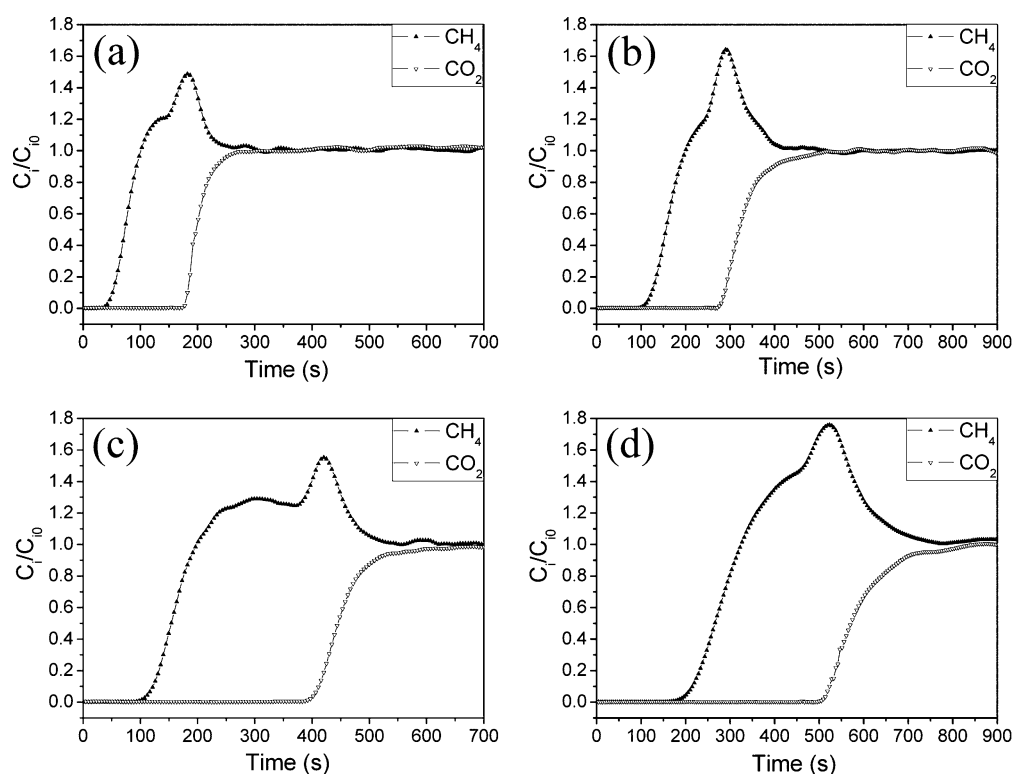**Figure 11.** Breakthrough curves of 50−50 mixture of CO_2−CH_4 at 303 K on the AlBDC$_{Micro}$ (a, 0.2 MPa; b, 0.4 MPa) and AlBDC$_{Meso}$ MOFs (c, 0.2 MPa; d, 0.4 MPa).

selectivities calculated from the breakthrough experiments are basically in agreement with the result of IGC. The little difference of CO_2/CH_4 selectivity obtained from two methods is due to the slight peak tail of CO_2 in IGC experiments.

Figure 11 shows the typical breakthrough curves of the 50−50 CO_2/CH_4 mixture on the AlBDC$_{Micro}$ and AlBDC$_{Meso}$ samples at 0.2 and 0.4 MPa, respectively. It should be noted that the filling quantity of AlBDC$_{Meso}$ particles is ca. 1.6 times that of AlBDC$_{Micro}$ particles in the adsorption bed with the same volume owing to the higher density of the AlBDC$_{Meso}$ particles (see Table 1). Thus, the adsorption account of the AlBDC$_{Meso}$ sample looks much higher than that of the AlBDC$_{Micro}$ sample in the same dynamic process, which does not affect the calculation of adsorption selectivity according to eq 1. From breakthrough curves in Figure 11, the adsorbance of CO_2 on the AlBDC$_{Micro}$ and AlBDC$_{Meso}$ MOFs was determined to be ca. 1.984 and 1.739 mmol/g at 2 bar and ca. 2.317 and 1.999 mmol/g at 4 bar, respectively. In the case of CH_4, the adsorbance on the AlBDC$_{Micro}$ MOF is ca. 0.174 mmol/g at 2 bar and 0.207 mmol/g at 4 bar, compared to 0.073 mmol/g at 2 bar and 0.088 mmol/g at 4 bar for the AlBDC$_{Meso}$ MOF. Clearly, the adsorbance of CO_2 on the AlBDC$_{Micro}$ MOF is slightly higher than that on the AlBDC$_{Meso}$ MOF, while the adsorbance of CH_4 on the AlBDC$_{Micro}$ MOF is 2 times more than that on the AlBDC$_{Meso}$ MOF. Similar results were also obtained from the CO_2 and CH_4 adsorption isotherms on the AlBDC$_{Micro}$ and AlBDC$_{Meso}$ MOFs, as shown in Figure S7 and Table S1 (Supporting Information). Obviously, the AlBDC$_{Meso}$ sample has a greater affinity towards CO_2 due to its high polarity and quadrupole, but the mesopore distribution will decrease greatly the adsorption potential of CH_4 on the Al-BDC MOF. In these curves, the elution of CH_4 always occurs first, while CO_2 was detected at the outlet after a longer time, as

expected. There is always a classical roll-up on the breakthrough curves of CH_4, which should be attributed to a thermal effect and the partial desorption of CH_4 due to the exothermic adsorption of CO_2. Generally, the roll-up may increase the uncertainty in the determination of the CH_4 adsorption quantity on adsorbents. Therefore, another experiment was carried out by a reported method to determine the accuracy of the calculation for CH_4 adsorption quantity,[23] revealing that the roll-up peak of the breakthrough curve of CH_4 will not affect the calculation of the adsorbed amount of CH_4 in our experiments.

The higher CO_2−CH_4 selectivities (see Table 4) of the AlBDC$_{Meso}$ MOFs are independent of the pressure, revealing that it would be a promising candidate for CH_4 separation from CH_4−CO_2 gas mixtures on the equilibrium effect. More specifically, the selectivity of the AlBDC$_{Meso}$ MOFs is much higher than that of the conventional activated carbons (ca. 2−6)[15,17,18] and also higher than the cases of some zeolites (<20) including ZSM-5, SAPO-34, and β,[10−13] but it is lower than that of zeolites 5A and 13X.[9] Compared with MOFs, the selectivity of AlBDC$_{Meso}$ MOFs is significantly higher than the case of MIL53-Al (ca. 8), MIL101-Al (<7), Cu-BTC (<10), ZIF-8 (<6), Uio-66 (ca. 4.5), and Mg-MOF-74 (ca. 8).[21−31] MIL53-Al, AlBDC$_{Micro}$, and AlBDC$_{Meso}$ MOFs are all constructed by the Al and carboxylate connectors, but the pore structure of the AlBDC$_{Meso}$ MOF is distinctive. Consequently, the AlBDC$_{Meso}$ MOF must have a relatively lower potential energy surface owing to the specific 1−4 nm pore size, which gives a lower affinity with CH_4. As it happens, the adsorbance of CH_4 in the AlBDC$_{Meso}$ MOFs decreases greatly with the increase of mesopores, which has been confirmed by the breakthrough curves and adsorption isotherms (as shown in Figure 11 and Figure S7, Supporting

Information). As a consequence, the AlBDC$_{Meso}$ MOF has a high selectivity for CO_2 over CH_4 without the adsorption heats increased significantly because of its expanding pore size, which makes it a good candidate for preferential adsorption of CO_2.

CONCLUSIONS

Al-BDC MOFs were prepared via a simple method fit for industrial use, and the pore size of Al-BDC MOFs was increased from 0.86 to 2.58 nm by a simplified washing and drying process. The results from structural analysis of the Al-BDC MOFs indicate that the decomposition of the BDC ligands in the AlBDC$_{Syn}$ crystals plays an important role in the formation of mesoporous structure. The AlBDC$_{Meso}$ with larger pore sizes prepared in this work has a very good selectivity in the separation of the CH_4/CO_2 mixtures, which was determined to be $\alpha_{CO2/CH4} \approx 24$ at 303 K in the range of pressures 0−1 MPa. It appears that Al-BDC MOFs will be a good alternative of activated carbons for the separation of CH_4 from the CH_4/CO_2 mixture. The initial heats of adsorption of CH_4 and CO_2 on the AlBDC$_{Meso}$ MOFs were determined to be 11.5 and 25.2 kJ mol^{-1} by the IGC method, respectively, which is significantly reduced by ca. 25% compared with that on the AlBDC$_{Micro}$ MOFs. The results indicate that the increase of pore size not only increases the selectivity of CO_2 adsorption over CH_4 but reduces the adsorption heat, revealing it should be the desired method to obtain a satisfactory absorbent for CO_2/CH_4 separation.

ASSOCIATED CONTENT

ⓢ Supporting Information

Figures S1−S7 and Table S1. This material is available free of charge via the Internet at http://pubs.acs.org.

AUTHOR INFORMATION

Corresponding Authors
*E-mail: suntianjun@dicp.ac.cn.
*E-mail: wangsd@dicp.ac.cn. Tel.: +86-411-84379052. Fax: +86-411-84662365.

Notes

The authors declare no competing financial interest.

ACKNOWLEDGMENTS

ABBREVIATIONS

C_i = concentration of component i in the gas phase (mol·m^{-3})

C_{i0} = initial concentration of concentration i in the gas phase (mol·m^{-3})

ΔH_{ads} = enthalpy of adsorption

K_c = sorption equilibrium constant based on sorbate concentration in a crystal

K_p = sorption equilibrium constant based on sorbate concentration in a pellet

L = length of the bed

m = mass of adsorbent

R = the gas constant

S = specific surface area of adsorbent

T_c = temperature of the bed

t_m = retention time of a nonadsorbing tracer (Helium)

t_R = retention time of a adsorbate

V_N = adsorbate net retention volumes

V_S = specific retention volume

Greek Alphabet

$\alpha_{i,j}$ = adsorption selectivity

v = interstitial gas velocity

ε = void fraction of the bed

θ = void fraction of pellet

REFERENCES

(1) Tagliabue, M.; Farrusseng, D.; Valenciac, S.; Aguado, S.; Ravon, U.; Rizzo, C.; Corma, A.; Mirodatos, C. Natural Gas Treating by Selective Adsorption: Material Science and Chemical Engineering Interplay. *Chem. Eng. J.* 2009, 155, 553−566.

(2) Bao, Z. B.; Yu, L.; Ren, Q. L.; Lu, X. Y.; Deng, Sh.G. Adsorption of CO_2 and CH_4 on a Magnesium-Based Metal Organic Framework. *J. Colloid Interface Sci.* 2011, 353, 549−556.

(3) Rufford, T. E.; Smart, S.; Watson, G. C. Y.; Graham, B. F.; Boxall, J.; DinizdaCostab, J. C.; May, E. F. The Removal of CO_2 and N_2 from Natural Gas: A Review of Conventional and Emerging Process Technologies. *J. Pet. Sci. Eng.* 2012, 94−95, 123−154.

(4) Yang, H. Q.; Xu, Z. H.; Fan, M. H.; Gupta, R.; Slimane, R. B.; Bland, A. E.; Wright, I. Progress in Carbon Dioxide Separation and Capture: A Review. *J. Environ. Sci.-China* 2008, 20, 14−27.

(5) Rao, A. B.; Rubin, E. S. A Technical, Economic, and Environmental Assessment of Amine-based CO_2 Capture Technology for Power Plant Greenhouse Gas Control. *Environ. Sci. Technol.* 2002, 36, 4467−4475.

(6) Aaron, D.; Tsouris, C. Separation of CO_2 from Flue Gas: A Review. *Sep. Sci. Technol.* 2005, 40, 321−348.

(7) Yeh, J. T.; Resnik, K. P.; Rygle, K.; Pennline, H. W. Semi-Batch Absorption and Regeneration Studies for CO_2 Capture by Aqueous Ammonia. *Fuel Process. Technol.* 2005, 86, 1533−1546.

(8) Cavenati, S.; Grande, C. A.; Rodrigues, A. E. Removal of Carbon Dioxide from Natural Gas by Vacuum Pressure Swing Adsorption. *Energy Fuels* 2006, 20, 2648−2659.

(9) Rolniak, P. D.; Kobayashi, R. Adsorption of Methane and Several Mixtures of Methane and Carbon Dioxide at Elevated Pressures and Near Ambient Temperatures on 5A and 13X Molecular Sieves by Tracer Perturbation Chromatography. *AIChE J.* 1980, 26, 616−625.

(10) Harlick, P. J. E.; Tezel, F. H. Adsorption of Carbon Dioxide, Methane and Nitrogen: Pure and Binary Mixture Adsorption for ZSM-5 with SiO$_2$/Al$_2$O$_3$ Ratio of 280. *Sep. Purif. Technol.* 2003, 33, 199−210.

(11) Heymans, N.; Alban, B.; Moreau, S.; DeWeireld, G. Experimental and Theoretical Study of the Adsorption of Pure Molecules and Binary Systems Containing Methane, Carbon Monoxide, Carbon Dioxide and Nitrogen: Application to the Syngas Generation. *Chem. Eng. Sci.* 2011, 66, 3850−3858.

(12) Huang, Z.; Xu, L.; Li, J. H.; Guo, G. M.; Wang, Y. Adsorption Equilibrium of Carbon Dioxide and Methane on β-Zeolite at Pressures of Up to 2000 kPa Using a Static Volumetric Method. *J. Chem. Eng. Data* 2010, 55, 2123−2127.

(13) Palomino, M.; Corma, A.; Jorda′, J. L.; Rey, F.; Valencia, S. Zeolite Rho: a Highly Selective Adsorbent for CO_2/CH_4 Separation Induced by a Structural Phase Modification. *Chem. Commun.* 2012, 48, 215−217.

(14) Himeno, S.; Komatsu, T.; Fujita, S. High-Pressure Adsorption Equilibria of Methane and Carbon Dioxide on Several Activated Carbons. *J. Chem. Eng. Data* 2005, 50, 369−376.

(15) Peng, X.; Wang, W.; Xue, R.; Shen, Z. Adsorption Separation of CH_4/CO_2 on Mesocarbon Microbeads: Experiment and Modeling. *AIChE J.* 2006, 52, 994−1003.

(16) Bai, B. C.; Cho, S.; Yu, H. R.; Yi, K. B.; Kim, K. D.; Lee, Y. S. Effects of Aminated Carbon Molecular Sieves on Breakthrough Curve Behavior in CO_2/CH_4 Separation. *J. Ind. Eng. Chem.* **2013**, *19*, 776−783.

(17) Buss, E. Gravimetric Measurement of Binary Gas Adsorption Equilibria of Methane-Carbon Dioxide Mixtures on Activated Carbon. *Gas Sep. Purif.* **1995**, *9*, 189−197.

(18) Goetz, V.; Pupier, O.; Guillot, A. Carbon Dioxide-Methane Mixture Adsorption on Activated Carbon. *Adsorption* **2006**, *12*, 55−63.

(19) Hao, S. Y.; Zhang, J.; Zhong, Y. J.; Zhu, W. D. Selective Adsorption of CO_2 on Amino-Functionalized Silica Spheres with Centrosymmetric Radial Mesopores and High Amino Loading. *Adsorption* **2012**, *18*, 423−430.

(20) Morishige, K. Adsorption and Separation of CO_2/CH_4 on Amorphous Silica Molecular Sieve. *J. Phys. Chem. C* **2011**, *115*, 9713−9718.

(21) Krishna, R. Adsorptive Separation of $CO_2/CH_4/CO$ Gas Mixtures at High Pressures. *Microporous Mesoporous Mater.* **2012**, *156*, 217−223.

(22) García, E. J.; Mowat, J. P. S.; Wright, P. A.; Pérez-Pellitero, J.; Jallut, C.; Pirngruber, G. D. Role of Structure and Chemistry in Controlling Separations of CO_2/CH_4 and $CO_2/CH_4/CO$ Mixtures over Honeycomb MOFs with Coordinatively Unsaturated Metal Sites. *J. Phys. Chem. C* **2012**, *116*, 26636−26648.

(23) Hamon, L.; Jolimaitre, E.; Pirngruber, G. D. CO_2 and CH_4 Separation by Adsorption Using Cu-BTC Metal-organic Framework. *Ind. Eng. Chem. Res.* **2010**, *49*, 7497−7503.

(24) Hamon, L.; Llewellyn, P. L.; Devic, T.; Ghoufi, A.; Clet, G.; Guillerm, V.; Pirngruber, G. D.; Maurin, G.; Serre, C.; Driver, G.; et al. Co-Adsorption and Separation of CO_2-CH_4 Mixtures in the Highly Flexible MIL-53(Cr) MOF. *J. Am. Chem. Soc.* **2009**, *131*, 17490−17499.

(25) Serra-Crespo, P.; Ramos-Fernandez, E. V.; Gascon, J.; Kapteijn, F. Synthesis and Characterization of an Amino Functionalized MIL-101(Al): Separation and Catalytic Properties. *Chem. Mater.* **2011**, *23*, 2565−2572.

(26) Abid, H. R.; Pham, G. H.; Ang, H. M.; Tade, M. O.; Wang, S. B. Adsorption of CH_4 and CO_2 on Zr-Metal Organic Frameworks. *J. Colloid Interface Sci.* **2012**, *366*, 120−124.

(27) Banerjee, R.; Furukawa, H.; Britt, D.; Knobler, C.; O'Keeffe, M.; Yaghi, O. M. Control of Pore Size and Functionality in Isoreticular Zeolitic Imidazolate Frameworks and Their Carbon Dioxide Selective Capture Properties. *J. Am. Chem. Soc.* **2009**, *131*, 3875−3877.

(28) Bourrelly, S.; Llewellyn, P. L.; Serre, C.; Millange, F.; Loiseau, T.; Férey, G. Different Adsorption Behaviors of Methane and Carbon Dioxide in the Isotypic Nanoporous Metal Terephthalates MIL-53 and MIL-47. *J. Am. Chem. Soc.* **2005**, *127*, 13519−13521.

(29) Finsy, V.; Ma, L.; Alaerts, L.; De Vos, D. E.; Baron, G. V.; Denayer, J. F. M. Separation of CO_2/CH_4 Mixtures with the MIL-53(Al) Metal-organic Framework. *Microporous Mesoporous Mater.* **2009**, *120*, 221−227.

(30) Llewellyn, P. L.; Bourrelly, S.; Serre, C.; Vimont, A.; Daturi, M.; Hamon, L.; Weireld, G. D.; Chang, J. S.; Hong, D. Y.; Hwang, Y. K.; et al. High Uptakes of CO_2 and CH_4 in Mesoporous Metal-Organic Frameworks MIL-100 and MIL-101. *Langmuir* **2008**, *24*, 7245−7250.

(31) Bae, Y. S.; Mulfort, K. L.; Frost, H.; Ryan, P.; Punnathanam, S.; Broadbelt, L. J.; Hupp, J. T.; Snurr, R. Q. Separation of CO_2 from CH_4 Using Mixed-Ligand Metal-organic Frameworks. *Langmuir* **2008**, *24*, 8592−8598.

(32) Yan, Q. J.; Lin, Y.Ch; Kong, Ch.L.; Chen, L. Remarkable CO_2/CH_4 Selectivity and CO_2 Adsorption Capacity Exhibited by Poly-amine-Decorated Metal-Organic Framework Adsorbents. *Chem. Commun.* **2013**, *49*, 6873−6875.

(33) Stylianou, K. C.; Warren, J. E.; Chong, S. Y.; Rabone, J.; Bacsa, J.; Bradshaw, D.; Rosseinsky, M. J. CO_2 Selectivity of a 1D Microporous Adenine-Based Metal-Organic Framework Synthesised in Water. *Chem. Commun.* **2011**, *47*, 3389−3391.

(34) Couck, S.; Denayer, J. F. M.; Baron, G. V.; Rémy, T.; Gascon, J.; Kapteijn, F. An Amine-Functionalized MIL-53 Metal-Organic Frame-work with Large Separation Power for CO_2 and CH_4. *J. Am. Chem. Soc.* **2009**, *131*, 6326−6327.

(35) Chen, Z. X.; Xiang, Sh.C.; Arman, H. D.; Li, P.; Zhao, D. Y.; Chen, B. L. Significantly Enhanced CO_2/CH_4 Separation Selectivity within a 3D Prototype Metal-Organic Framework Functionalized with OH Groups on Pore Surfaces at Room Temperature. *Eur. J. Inorg. Chem.* **2011**, *14*, 2227−2231.

(36) Bae, Y. S.; Hauser, B. G.; Farha, O. K.; Hupp, J. T.; Snurr, R. Q. Enhancement of CO_2/CH_4 Selectivity in Metal-Organic Frameworks Containing Lithium Cations. *Microporous Mesoporous Mater.* **2011**, *141*, 231−235.

(37) Shang, J.; Li, G.; Singh, R.; Gu, Q. F.; Nairn, K. M.; Bastow, T. J.; Medhekar, N.; Doherty, C. M.; Hill, A. J.; Liu, J. Z.; Webley, P. A. Discriminative Separation of Gases by a "Molecular Trapdoor" Mechanism in Chabazite Zeolites. *J. Am. Chem. Soc.* **2012**, *134*, 19246−19253.

(38) Schubert, M.; Mueller, U.; Tonigold, M.; Ruetz, R. Method for Producing Organometallic Framework Materials Containing Main Group Metal Ions. Patent US 20100166644A1. 2010.

(39) Bezverkhyy, I.; Ortiz, G.; Chaplais, G.; Marichal, C.; Weber, G.; Bellat, J. P. MIL-53(Al) under reflux in water: Formation of c-AlO(OH) shell and H_2BDC molecules intercalated into the pores. *Microporous Mesoporous Mater.* **2014**, *183*, 156−161.

(40) Loiseau, T.; Serre, C.; Huguenard, C.; Fink, G.; Taulelle, F.; Henry, M.; Bataille, T.; Férey, G. A Rationale for the Large Breathing of the Porous Aluminum Terephthalate (MIL-53) Upon Hydration. *Chem.—Eur. J.* **2004**, *10*, 1373−1382.

(41) Thielmann, F. Introduction into the Characterisation of Porous Materials by Inverse Gas Chromatography. *J. Chromatogr. A* **2004**, *1037*, 115−123.

(42) Bagreev, A.; Bandosz, T. J. Study of Hydrogen Sulfide Adsorption on Activated Carbons using Inverse Gas Chromatography at Infinite Dilution. *J. Phys. Chem. B* **2000**, *104*, 8841−8847.

(43) Shah, D. B.; Ruthven, D. M. Measurement of Zeolitic Diffusivities and Equilibrium Isotherms by Chromatography. *AIChE J.* **1977**, *23*, 804−809.

(44) Conder, J. R.; Young, C. L. *Physicochemical Measurement by Gas Chromatography*; John Wiley & Sons: New York, 1979.

(45) Mollmer, J.; Lange, M.; Moller, A.; Patzschke, C.; Stein, K.; Lassig, D.; Lincke, J.; Glaser, R.; Krautscheid, H.; Staudt, R. Pure and Mixed Gas Adsorption of CH_4 and N_2 on the Metal-Organic Framework Basolite A100 and a Novel Copper-Based 1,2,4-Triazolyl Isophthalate MOF. *J. Mater. Chem.* **2012**, *22*, 10274−10286.